

Proposal: 5-32-787 **Council:** 10/2012

Title: Magnetization reversal in cobalt and nickel nanowire arrays

This proposal is a new proposal

Research Area: Materials

Main proposer: MICHELS ANDREAS

Experimental Team: BICK Jens-Peter
 GUENTHER Annegret
 MALYEV Artem
 SZARY Philipp

Local Contact: DEWHURST Charles

Samples: Co in Al₂O₃
 Ni in Al₂O₃

Instrument	Req. Days	All. Days	From	To
D33	5	5	05/04/2013 01/07/2013	09/04/2013 02/07/2013

Abstract:

Using spin-resolved SANS (POLARIS), we will investigate the magnetization-reversal process of Co and Ni nanowire arrays. Since the magnetization reversal is largely determined by transversal spin components, we aim at extracting the ensuing spin-misalignment SANS cross section through measurement of the spin-flip cross section. The proposed spin-resolved SANS experiments will provide insights into the size of the characteristic length scales during magnetization reversal. More specifically, we expect to answer the questions whether the reversal takes place "wire by wire" or in a more cooperative fashion and what is the size of the magnetically perturbed region relative to the structural size of the wires (length, diameter).

Magnetization reversal of a Co nanowire array

Annegret Günther, Jens-Peter Bick, Philipp Szary and Andreas Michels

Physics and Materials Science Research Unit, University of Luxembourg, L-1511 Luxembourg, Luxembourg

Charles Dewhurst

Institut Laue-Langevin, F-38042 Grenoble Cedex 9, France

Pulsed electrodeposition of Cobalt into a nanoporous aluminum oxide layer results in an ordered Co nanorod array. The nanorods with average diameter $d \approx 27 \pm 3$ nm and length $l \approx 480 \pm 45$ nm are hexagonally arranged with a center-to-center distance of the rods of $d_{CC} \approx 48 \pm 5$ nm [fig. 1 (a)]. Magnetization measurements reveal that the rods have a pronounced shape anisotropy with the easy axis along the long rod axis [fig. 1 (b)].

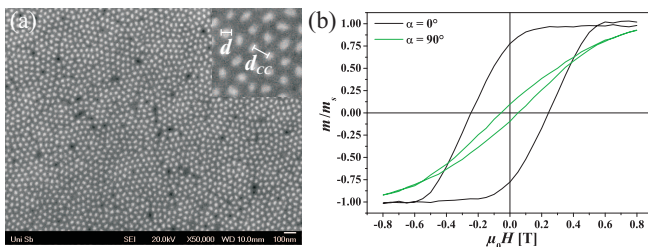


Figure 1: (a) SEM top view of the Co nanorod array. The white circles are the end faces of the nanorods. (b) Magnetization measurements of the array, with α being the angle between the applied magnetic field \mathbf{H} and the long rod axes.

Such an array can be considered as a model system for a ferromagnetic nanorod arrangement. In order to probe the relevant length scales of the magnetic microstructure of the array during the magnetization-reversal process, we performed magnetic-field-dependent SANS on D33; we used an incident wavelength of $\lambda = 8$ Å and two sample-to-detector distances of 12.8 m and 2.5 m with corresponding collimation lengths, resulting in an accessible q -range of $0.03 \text{ nm}^{-1} \lesssim q \lesssim 1.3 \text{ nm}^{-1}$.

Magnetic-field-dependent measurements were carried out at room temperature by first applying a large positive field ($\mu_0 H = 2$ T), which is assumed to saturate the sample, and then reducing the field to the experimental value (following the magnetization curve). This procedure was executed for two different scattering geometries, i.e., the long rod axes were aligned parallel to the incident neutron beam and *perpendicular* to the applied magnetic field ($\mathbf{H} \perp \mathbf{k}_i$ geometry) and the long rod axes were aligned parallel to the incident neutron beam and *parallel* to the applied magnetic field ($\mathbf{H} \parallel \mathbf{k}_i$ geometry).

The detected differential SANS cross sections $d\Sigma/d\Omega$

of the Co nanorod array for the two scattering geometries are shown in fig. 2 for selected applied magnetic fields between saturation (left images) and the respective coercive fields (right images).

At saturation in $\mathbf{H} \perp \mathbf{k}_i$ geometry, an intensity ring occurs with maxima perpendicular to \mathbf{H} (seen as two dark-red half moons, fig. 2 (a), left). With decreasing magnetic field, scattering due to transversal spin components emerges at smaller q and a maximum (overall) intensity can be observed at the coercive field $\mu_0 H_C = -0.05$ T (fig. 2 (a), right). The same behaviour is detected in $\mathbf{H} \parallel \mathbf{k}_i$ geometry [fig. 2 (b)], except that the scattering at saturation (fig. 2 (b), left) is isotropically distributed on the ring.

The intensity rings, which occur in both scattering geometries, arise from the fact that the hexagonal order of the rods is not perfect over the whole scattering volume, but rather restricted to domains with a size of a few hundred nanometers. This gives rise to Debye-Scherrer diffraction rings.

The half-moon intensity maxima in $\mathbf{H} \perp \mathbf{k}_i$ geometry are due to the $\sin^2 \theta$ -dependence of the SANS cross section at saturation [1]:

$$\frac{d\Sigma_{\perp, \text{sat}}}{d\Omega}(\mathbf{q}) \propto |\tilde{N}(\mathbf{q})|^2 + |\tilde{M}_z(\mathbf{q})|^2 \sin^2 \theta, \quad (1)$$

with $\tilde{N}(\mathbf{q})$ and $\tilde{M}_z(\mathbf{q})$ representing the nuclear and the magnetic scattering amplitudes, respectively. By contrast, for the $\mathbf{H} \parallel \mathbf{k}_i$ geometry, the SANS cross section at saturation is given as [2],

$$\frac{d\Sigma_{\parallel, \text{sat}}}{d\Omega}(\mathbf{q}) \propto |\tilde{N}(\mathbf{q})|^2 + |\tilde{M}_z(\mathbf{q})|^2. \quad (2)$$

The resulting radially-averaged data of the differential SANS cross sections of the Co nanorod array are shown in fig. 3. The intensity rings, observed in both geometries in the 2D detector images at 2 T, can be identified in the radially-averaged data (black open squares in fig. 3) as the low- q peak at $q_1 \cong 0.14 \text{ nm}^{-1}$ ($2\pi/q_1 \cong 45$ nm). Moreover, two additional peaks were detected at higher q -values ($q_2 \cong 0.25 \text{ nm}^{-1}$ and $q_3 \cong 0.38 \text{ nm}^{-1}$), which can also be related to the hexagonal order of the pores.

At smaller $q \lesssim 0.1 \text{ nm}^{-1}$, the scattering intensities

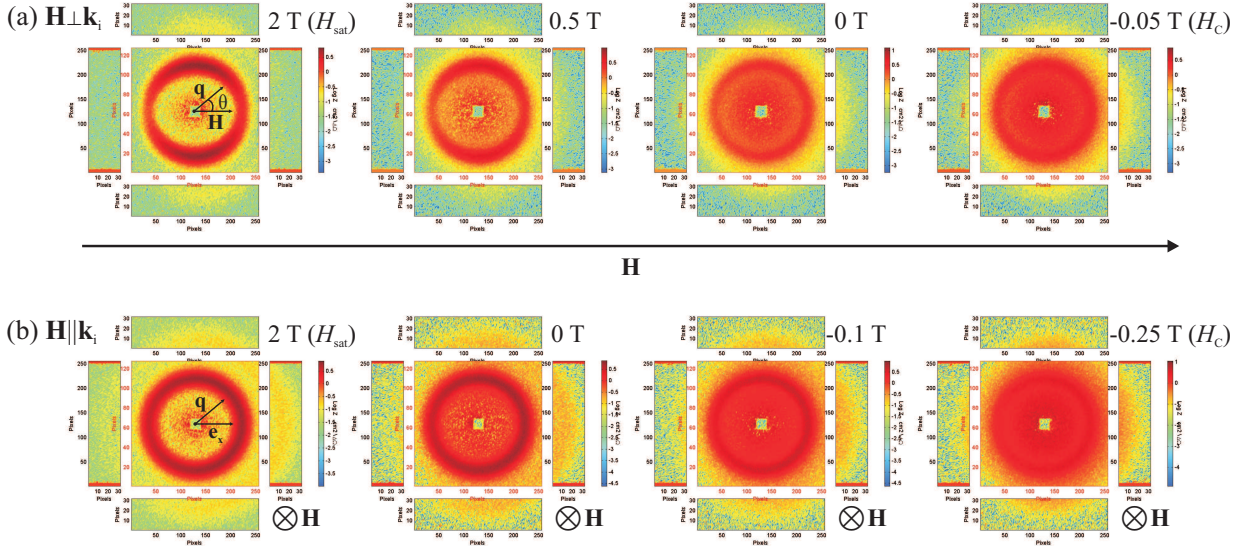


Figure 2: SANS cross sections $d\Sigma/d\Omega$ on the 2D area detector for selected applied magnetic fields (see insets). (a) $\mathbf{H} \perp \mathbf{k}_i$; (b) $\mathbf{H} \parallel \mathbf{k}_i$.

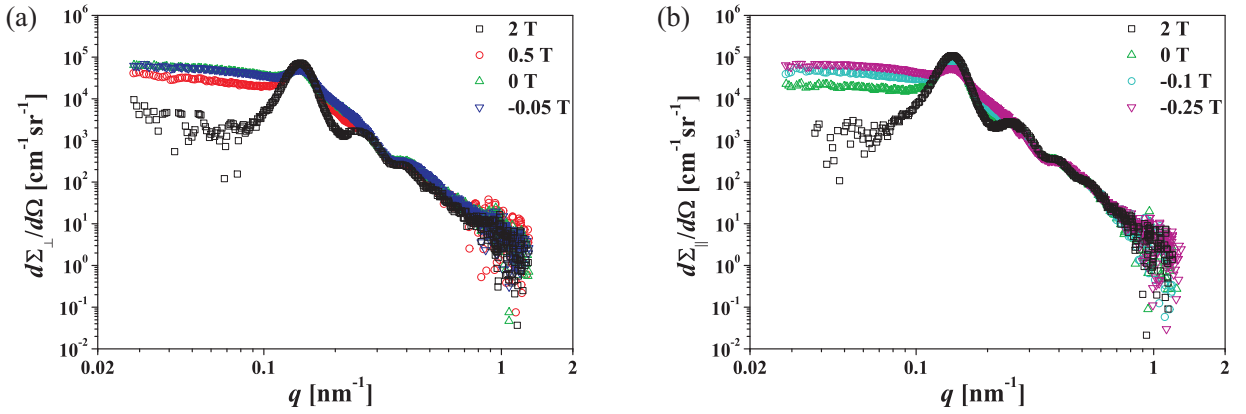


Figure 3: Radially-averaged scattering cross sections $d\Sigma/d\Omega$ as a function of momentum transfer q and at selected applied magnetic fields H (see insets) for (a) $\mathbf{H} \perp \mathbf{k}_i$ and for (b) $\mathbf{H} \parallel \mathbf{k}_i$.

in both geometries increase with decreasing magnetic field. This is due to the additional scattering contribution of the transversal magnetization (spin-misalignment) components \tilde{M}_x and \tilde{M}_y (see refs. [1] and [2]). The total intensity in the first Bragg peak is reduced and washed out with decreasing field.

Radially-averaging of the scattering cross section at saturation (2 T) in $\mathbf{H} \perp \mathbf{k}_i$ geometry $d\Sigma_{\perp, \text{sat}}/d\Omega$ [see eq. (1)] results in

$$\frac{d\Sigma_{\perp, \text{sat}}}{d\Omega}(q) \propto |\tilde{N}(q)|^2 + \frac{1}{2}|\tilde{M}_z(q)|^2, \quad (3)$$

whereas for $\mathbf{H} \parallel \mathbf{k}_i$ geometry eq. (2) holds for radially-averaging of $d\Sigma_{\parallel, \text{sat}}/d\Omega$. By combining eq. (3) and eq. (2), it is possible to separate the nuclear from magnetic SANS:

$$|\tilde{N}(q)|^2 \propto 2 \cdot \frac{d\Sigma_{\perp, \text{sat}}}{d\Omega}(q) - \frac{d\Sigma_{\parallel, \text{sat}}}{d\Omega}(q), \quad (4)$$

$$|\tilde{M}_z(q)|^2 \propto \frac{d\Sigma_{\parallel, \text{sat}}}{d\Omega}(q) - |\tilde{N}(q)|^2. \quad (5)$$

The in this way determined experimental nuclear $|\tilde{N}(q)|^2$ and magnetic $|\tilde{M}_z(q)|^2$ SANS cross sections are shown in fig. 4 together with $d\Sigma_{\parallel, \text{sat}}/d\Omega(q)$.

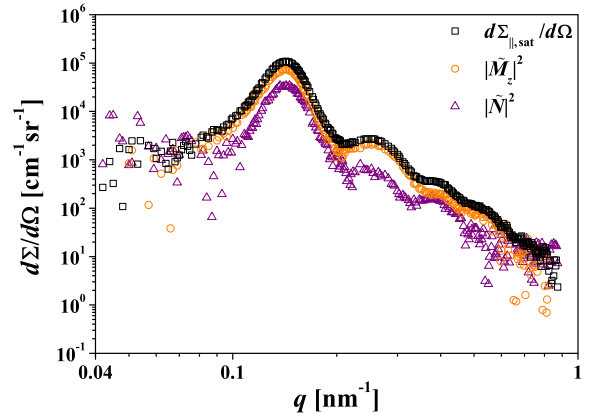


Figure 4: Nuclear $|\tilde{N}|^2$ and magnetic $|\tilde{M}_z|^2$ scattering cross sections as well as $d\Sigma_{\parallel, \text{sat}}/d\Omega$ as a function of momentum transfer q .

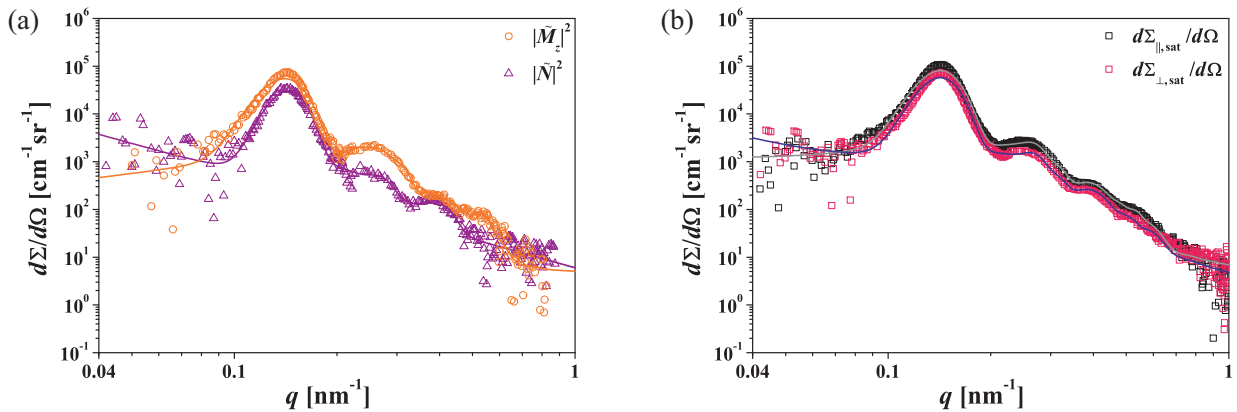


Figure 5: (a) Nuclear $|\tilde{N}|^2$ and magnetic $|\tilde{M}_z|^2$ scattering cross sections as well as (b) $d\Sigma_{||,\text{sat}}/d\Omega$ and $d\Sigma_{\perp,\text{sat}}/d\Omega$ as functions of momentum transfer q . Solid lines are data fits to eq. (6).

	$ \tilde{M}_z ^2$	$ \tilde{N} ^2$	$d\Sigma_{ ,\text{sat}}/d\Omega$	$d\Sigma_{\perp,\text{sat}}/d\Omega$
R [nm]	15.9 ± 0.1	15.0 ± 0.3	15.4 ± 0.1	15.4 ± 0.1
d_{CC} [nm]	49.7 ± 0.3	49.2 ± 0.3	49.3 ± 0.2	49.4 ± 0.2

Table 1: Resulting structural parameters from fitting the nuclear $|\tilde{N}|^2$ and magnetic $|\tilde{M}_z|^2$ SANS cross sections as well as the SANS data at saturation for both scattering geometries $d\Sigma_{||,\text{sat}}/d\Omega$ and $d\Sigma_{\perp,\text{sat}}/d\Omega$ with eq. (6). R is the rod radius and d_{CC} the center - to - center distance of the rods in the alumina layer.

The resulting ratio of the experimentally determined nuclear to magnetic scattering $|\tilde{N}|^2/|\tilde{M}_z|^2 \approx 0.5 \pm 0.2$ is in good agreement with the theoretically calculated value of the nuclear - to - magnetic scattering length - density contrast $(\Delta\rho)_{\text{nuc}}^2/(\Delta\rho)_{\text{mag}}^2 \approx 0.7$.

For the quantitative description of the nuclear $|\tilde{N}|^2$ and magnetic $|\tilde{M}_z|^2$ SANS cross sections [fig. 5 (a)], as well as the SANS data at saturation ($\mu_0 H = 2$ T) [fig. 5 (b)], we consider a magnetic - field - independent model $I(q)$ by combining the structure factor $S(q)$ of a 2D hexagonal lattice with the form factor $F(q)$ of a cylinder,

$$I(q) = I_{\text{inc}} + S(q)|F(q)|^2, \quad (6)$$

where I_{inc} denotes the incoherent scattering background. The cylinder form factor for \mathbf{q} perpendicular to the long rod axes is given by $F(q) = 2J(1, qR)/qR$, where $J(1, qR)$ is the spherical Bessel function of first order with $R = d/2$ being the rod radius. The structure factor is assumed as a sum of Gaussians, $S(q) = \sum_i a_i / \sqrt{2\pi\sigma_i^2} \exp(-(q - q_i)^2/2\sigma_i^2)$, with the Bragg peak positions from the 2D hexagonal lattice at $q_i = \frac{4\pi}{d_{CC}\sqrt{3}} \cdot \sqrt{h^2 + k^2} + hk$, where $(hk) = (10), (11), (20), (21), (30)$ and (22) . The data fits by this model are the solid lines in fig. 5.

The resulting values of the structural fit parameters are listed in table 1 and are in good agreement with each other as well as consistent with the results from

electron microscopy, which are $R \approx 13.5 \pm 1.5$ nm and $d_{CC} \approx 48 \pm 5$ nm.

In future work the above model will be extended in order to describe the magnetic - field - dependence of the SANS cross sections during the magnetization - reversal process and to extract in this way the characteristic length scales of the magnetic microstructure.

References

- [1] A. Michels and J. Weissmüller, Magnetic - field - dependent small - angle neutron scattering on random anisotropy ferromagnets, *Reports on Progress in Physics* **71**, 066501 (2008).
- [2] A. Michels, D. Honecker, F. Döbrich, C. D. Dewhurst, A. Wiedenmann, C. Gómez - Polo and K. Suzuki, Small - angle Neutron Scattering with One - dimensional Polarization Analysis, *Neutron News* **22**, 15 (2011).